ECS Journal of Solid State Science and Technology, 2024 **13** 073010

Synthesis and Tuning of Electronic, Optical, and Photoelectrochemical Properties of Copper Metavanadate Alloys via Alkaline Earth Metal Substitution

Fahad I. Danladi,[1] Abhishek Rawat,[1] Abhishek Kumar Adak,[2] Chuzhong Zhang,[3] Vinod K. Sangwan,[4] Riddhi Ananth,[4] Mark C. Hersam,[4,*] Efstathios I. Meletis,[3] and Krishnan Rajeshwar[1,*,z]

[1]*Department of Chemistry & Biochemistry, The University of Texas at Arlington, Arlington, Texas 76019, United States of America*
[2]*The Abdus Salam International Centre for Theoretical Physics (ICTP), 34151 Trieste, Italy*
[3]*Department of Materials Science and Engineering, The University of Texas at Arlington, Arlington, Texas 76019, United States of America*
[4]*Department of Materials Science and Engineering, Northwestern University, Evanston, Illinois 60208, United States of America*

Unlike the well-studied and technologically advanced Group III-V and Group II-VI compound semiconductor alloys, alloys of ternary metal oxide semiconductors have only recently begun to receive widespread attention. Here, we describe the effect of alkaline earth metal substitution on the optical, electronic, and photoelectrochemical (PEC) properties of copper metavanadate (CuV_2O_6). As a host, the Cu-V-O compound family presents a versatile framework to develop such composition-property correlations. Alloy compositions of $A_{0.1}Cu_{0.9}V_2O_6$ (A = Mg, Ca) photoanodes were synthesized via a time and energy-efficient solution combustion synthesis (SCS) method. The effect of introducing alkaline earth metals (Mg, Ca) on the crystal structure, microstructure, electronic, and optical properties of copper metavanadates was investigated by powder X-ray diffraction (PXRD), scanning electron microscopy (SEM), diffuse reflectance spectroscopy (DRS), transmission electron microscopy (TEM), and Raman spectroscopy. The PXRD, TEM, and Raman spectroscopy data demonstrated the polycrystalline powder samples to be mutually soluble, solid solutions of copper and alkaline earth metal metavanadates and not simple mixtures of these compounds. The DRS data showed a systematic decrease in the optical bandgap with Cu incorporation. These trends were corroborated by electronic band structure calculations. Finally, the PEC properties exhibited a strong dependence on the alloy composition, pointing to possible applicability in solar water splitting, heterogeneous photocatalysis, phosphor lighting/displays, and photovoltaic devices.
 [DOI: 10.1149/2162-8777/ad5b88]

Manuscript submitted March 22, 2024; revised manuscript received June 15, 2024. Published July 19, 2024.

Supplementary material for this article is available online

This companion study to a recent paper[1] from our collaborative team, focuses on a new $A_{0.1}Cu_{0.9}V_2O_6$ (A = Mg, Ca) alloy system. Alloys offer a promising avenue for enhancing materials performance, and many examples exist for how Group III-V and II-VI compound semiconductors have revolutionized human life quality, e.g., via devices including lasers, displays, night vision technology, solar cells etc. On the other hand, alloys derived from metal oxide semiconductors (especially, ternary oxides) have only recently begun to be explored.

Examples of recent research on ternary oxide solid solutions include $(Ba_{1-x}Sn_x)ZrO_3$,[2] $M_2V_2O_7$ (M = Mn, Cu),[3] $Eu_{1-x}Ca_xTiO_3$,[4] $(Cu_{1-x}Li_x)GaO_2$,[5] $(Bi_{1-x}Fe_x)VO_4$,[6] $(Li_{1-x}Cu_x)Nb_3O_8$,[7] $M_xBi_{2-x}Ti_2O_7$ (M = Fe, Mn),[8] $BiZn_2VO_6$,[9] $BiCu_2VO_6$,[10] and $Cu_5(Ta_{1-x}Nb_x)_{11}O_{30}$.[11] Combinatorial synthesis combined with photoelectrochemical (PEC) screening was used to develop Cu-V-M-O (M = Mg, Ca, Sr, Fe) compositions[12] and to alloy β-$Cu_2V_2O_7$ with six cations.[13] Very recently, the electrocatalytic properties of a range of oxygen-deficient $Ca_3Fe_{3-x}Mn_xO_8$ (x = 1–2) alloys were described in this journal.[14] These perovskites do not appear to be semiconductors, however; their electronic band structures were not explored in Ref. 14 unlike in the families of oxides identified above.

Our prior experience[1,15,16] with the Cu-V-O compound family had bolstered the notion that Cu incorporation would lower the energy bandgap and thereby improve visible light absorption of the vanadium oxide parent framework. In this paper, as in our companion report,[1] we develop this theme further both experimentally and theoretically and explore the added effect of alkaline metal incorporation specifically into the CuV_2O_6 host framework. New data on alloying with Ca are presented here along with the Mg alloy previously reported[1] for the CuV_2O_6 host framework.

The corresponding property variations were expanded to include structural and morphological aspects of the alloys in both the Ca and Mg cases. As in our previous report,[1] these alloys were synthesized by solution combustion synthesis (SCS), a hitherto unprecedented synthesis candidate for ternary copper vanadates except in our group. Thus, the SCS of the copper end member (CuV_2O_6) as well as the magnesium end member (MgV_2O_6) was described by us previously.[1] The level of alkaline earth metal (A) incorporation was kept below ~10% in this study so as not to exceed the limit of solubility of the "foreign" cation, A as borne out by preliminary experiments.

Experimental and Theoretical Methods

Materials.—All the chemicals: $Cu(NO_3)_2{\cdot}2.5H_2O$, (Alfa Aesar), $Mg(NO_3)_2{\cdot}6H_2O$ (99+%, Acros Organics), $Ca(NO_3)_2{\cdot}4H_2O$ (Certified ACS, Fisher Scientific), NH_4VO_3 (Alfa Aesar), $C_4H_6O_5$ (98%, Alfa Aesar), NH_4OH (Alfa Aesa), HCOONa (Kodak), H_3BO_3 (Fisher Scientific) and $Na_2B_4O_7{\cdot}10H_2O$, were used without further purification.

Solution combustion synthesis.—The metavanadates were prepared via solution combustion synthesis following the chemical reaction shown in Eq. 1.

$$3M(NO_3)_2{\cdot}xH_2O_{(s)} + 6NH_4VO_{3(s)} + C_4H_6O_{5(s)} \rightarrow 3MV_2O_{6(s)} + 6N_{2(g)} + 4CO_{2(g)} + (15 + 3x)H_2O_{(g)} \quad [1]$$

where, M = Mg, Ca, Cu.

*Electrochemical Society Fellow.
[z]E-mail: rajeshwar@uta.edu

All the polycrystalline samples were prepared by SCS according to the procedure from our previous report.[15] The end members MgV_2O_6, CaV_2O_6, CuV_2O_6, and the solid solutions $A_{0.1}Cu_{0.9}V_2O_6$ (A = Mg, Ca) were prepared by dissolving a stoichiometric amount of alkaline earth metal or copper nitrates, ammonium vanadate and DL-malic acid in a beaker containing water as per Table I. After ultrasonic homogenization, the mixture was placed in a preheated muffle furnace at ~300 °C for 5–10 min, where it was first dehydrated before ignition. All samples were subsequently annealed at 600 °C for 1 h in an alumina crucible to improve sample crystallinity and remove organic (i.e., carbonaceous) traces from the combustion step. The anneal temperature was established after thermal analyses after carefully considering phase stability trends by differential scanning calorimetry and thermogravimetry.

Physical characterization.—Samples were analyzed by powder X-ray diffraction using a Bruker D8 advance instrument (Cu Kα radiation: $\lambda = 1.5406$ Å). The samples were measured at 40 kV and 40 mA over a 2θ range of 10–60° with a step size of $2\theta = 0.02°$ and scan speed of 1° per minute. Phase analyses and Rietveld refinement of the PXRD data was carried out using GSAS-EXPGUI software package.[17] Transmission electron microscopy (TEM) was carried out using Hitachi H-9500 instrument operating at an acceleration voltage of 300 kV and a LaB_6 filament. Scanning electron microscopy (SEM) and energy dispersive X-ray analysis (EDX) were performed on a Hitachi S-3000 N field emission scanning electron microscope equipped with a tungsten electron source and Thermo Scientific UltraDry^{TM} model detector. Samples were coated on conductive carbon grids for this purpose. Spectral data for EDX elemental mapping were recorded at an accelerating voltage of 25 kV.

Raman spectra of the samples were collected on a Thermo Scientific DXR3 Raman microscope equipped with a 633 nm diode laser (He-Ne gas laser) at 1 mW power output. Diffuse reflectance spectroscopy (DRS) was carried out on a Varian Cary 500 instrument and over the wavelength range, 350–800 nm. The absorption coefficient, α, was calculated from Kubelka—Munk transformation (Eq. 2) of the reflectance data.[18,19]

$$\frac{\propto}{S} = \frac{(1-R)^2}{2R} \qquad [2]$$

Here, α is the absorption coefficient, S is the scattering coefficient and R represents the reflectance. Optical bandgaps were estimated using the Tauc analyses in Eq. 3.[18–21]

$$h\nu = \propto (h\nu - E_g)^n \qquad [3]$$

where E_g is the bandgap and the parameter n describes the nature of the optical transition, i.e., n = ½ for a direct allowed transition and n = 2 for an indirect allowed transition.

A Thermo NEXSA instrument equipped with an Al Kα X-ray source was used for X-ray photoelectron spectroscopy (XPS). Inductively coupled plasma-atomic emission spectroscopy (ICP-AES) was performed on a Thermo iCap7600 instrument equipped with radial view and an ESI SC-2DX PrepFAST autosampler. Online dilution process was carried out using a prepFAST system, and standards for Cu, Mg, Ca, and V with concentrations ranging from 0.5 ppm to 10 ppm were used to create calibration curves. A slight modification to the standard digestion method was required to dissolve the vanadium oxide precipitate, and involved the addition of 500 μl of concentrated hydrochloric acid and heating overnight at 65 °C.

Electrode preparation and photoelectrochemical measurements.—Electrode films were prepared by suspending 100 mg of the bulk powder in 20 ml of ethanol and deposited on fluorine-doped tin oxide (FTO) by spray-coating using a previously reported procedure.[22] Specifically, the homogeneity of sample loading was maintained by adjusting the spray gun normal to the designated area of FTO and spraying at constant intervals. Electron microscopy and EDX were used to confirm elemental distribution, texture and surface homogeneity of these coatings. Photoelectrochemical (PEC) measurements were performed using a CH Instruments, Model CHI720C potentiostat. The surface of the working electrodes was irradiated with a 400 W Xe-arc lamp (Newport) equipped with an IR filter. A calibrated Si reference cell (Oriel) was used to achieve a measured light intensity of 1 Sun (100 mW cm^{-2}). All PEC measurements were carried out in a standard one-compartment, three-electrode quartz electrochemical cell format, where Ag/AgCl/3 M NaCl was used as the reference electrode, a Pt wire as the counter electrode, and the FTO-supported vanadate film as the working electrode. Potential conversion to the reversible (normal) hydrogen electrode (NHE) scale was accomplished according to Eq. 4.

$$E_{RHE} = E_{Ag/AgCl} + E^0_{Ag/AgCl(3\ M\ KCl)} + 0.0591pH \qquad [4]$$

where $E^0_{Ag/AgCl(3\ M\ KCl)} = 0.209$ V vs NHE at 25 °C.

Photoelectrochemical measurements of the vanadate films were performed in a 0.1 M borate buffer electrolyte (pH = 8.0) using potentiodynamic scans at 5 mV s^{-1} sweep rate. In some cases, 4 M formate was added to the electrolyte as a hole scavenger. Front-side illumination with a manual chopper was used at intervals of 5 s.

Computational methodology.—Spin-polarized *ab initio* density functional theory (DFT) calculations were performed as implemented in the Quantum ESPRESSO package.[23,24] To expand the Kohn–Sham equations, a plane wave basis set was employed with kinetic energy cut-off of 50 Ry for the electronic wave functions. Projector-augmented wave (PAW) potentials[25] were used to describe the interactions between the ionic core and the valence electrons. The revised Perdew–Burke–Ernzerhof (PBE) functional within the generalized gradient approximation (GGA) for solids, namely the PBEsol functional was utilized to describe the electron exchange and correlation.[26] The Brillouin zone was sampled using a Monkhorst–Pack k-point mesh.[27]

Geometry optimization of CaV_2O_6 was performed using an unshifted k-point mesh of 4 × 12 × 6, while the geometry optimization of bulk CuV_2O_6 and MgV_2O_6 utilized an unshifted k-point mesh of 4 × 10 × 6. To calculate the projected density of states (PDOS), a denser k-point grid was employed. To aid convergence, a

Table I. The concentration of precursor mixtures for the synthesis of end members and solid solutions via SCS.

	Precursor mixture composition (M)				
Sample	$Mg(NO_3)_2.6H_2O$	$Ca(NO_3)_2.4H_2O$	$Cu(NO_3)_2.6H_2O$	NH_4VO_3	$C_4H_6O_5$
MgV_2O_6	0.250	0.000	0.000	0.500	0.750
CaV_2O_6	0.000	0.250	0.000	0.500	0.750
$Mg_{0.1}Cu_{0.9}V_2O_6$	0.025	0.000	0.225	0.500	0.750
$Ca_{0.1}Cu_{0.9}V_2O_6$	0.000	0.025	0.225	0.500	0.750
CuV_2O_6	0.000	0.000	0.250	0.500	0.750

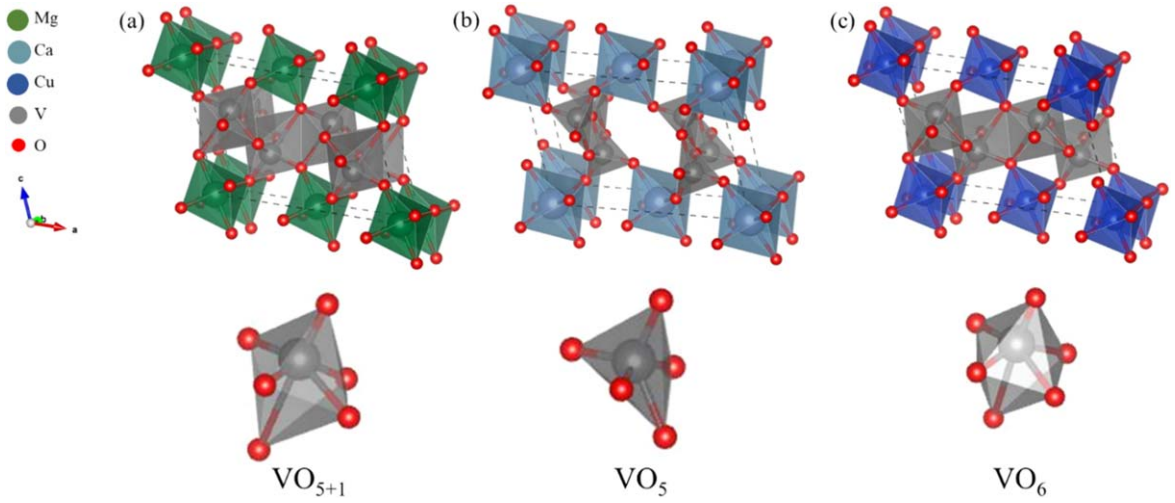

Figure 1. Crystal structures for (a) MgV_2O_6, (b) CaV_2O_6 and (c) CuV_2O_6 with their respective VO_n polyhedral units.

Table II. Comparison of ICP-AES assays with precursor SCS solution makeup.

	Experimental ratio			Precursor ratio		
Sample	Cu/2 V	Mg/2 V	Ca/2 V	Cu/2 V	Mg/2 V	Ca/2 V
MgV_2O_6	0.00	1.05	0.00	0.00	1.00	0.00
CaV_2O_6	0.00	0.00	1.02	0.00	0.00	1.00
CuV_2O_6	1.05	0.00	0.00	1.00	0.00	0.00
$Mg_{0.1}Cu_{0.9}V_2O_6$	0.95	0.11	0.00	0.90	0.10	0.00
$Ca_{0.1}Cu_{0.9}V_2O_6$	0.96	0.00	0.11	0.90	0.00	0.10

Marzari-Vanderbilt[28] cold smearing function with a width of 0.005 Ry was used. Hellmann-Feynman forces[29] were employed to allow relaxation of all atoms inside a unit cell until the residual forces on all the constituent atoms decreased below 0.01 eV Å.

DFT has a well-known limitation of underestimating the self-interaction correction (SIC) for strongly correlated electrons in highly localized orbitals. Therefore, to better describe the localization of the 3*d* electrons of Cu and V, a DFT + U framework[30] was employed in this study. Within this framework, the on-site Coulombic interaction term U and exchange parameter J were the main controlling factors to manipulate the SIC, leading to an enhanced depiction of the geometric, electronic, and magnetic structures. Values for U of 3.0 eV and 3.5 eV, respectively, were used for the Cu and V 3*d* orbitals, with a fixed value of J set at 1 eV for better alignment with the experimentally observed lattice parameters, energy band gaps, and magnetic ordering of the investigated systems. Analogous U values were employed for Cu and V 3*d* orbitals in many oxide compounds, as previously reported in the literature.[16,31,32]

Results and Discussion

Crystal structure and chemical/phase composition.—The MV_2O_6 (M = Mg, Ca, Cu) compound family crystallizes in brannerite (monoclinic, m-brannerite and triclinic, t-brannerite) or pseudobrannerite (p-brannerite) structure types.[33,34] MgV_2O_6 exhibits a m-brannerite structure (Fig. 1a) consisting of MgO_6 octahedra that form $(Mg\text{-}O)_n$ chains along the b-axis and edge-shared VO_6 octahedra which form infinite anionic layers along the ac-plane.[33] The vanadium ions have 5 + 1 coordination with one of the V-O bond lengths being much longer than the others in the VO_6 octahedra.[33] The MgO_6 octahedra are sandwiched between layers of $(VO_6)_n$ to form infinite chains along the b-axis.[33] The m-brannerite structure transforms to a p-brannerite structure by rotation of $(V\text{-}O)_n$ zig-zag chains around the b-axis, such that one of the most weakly bonded V-O bonds will elongate and change the coordination of vanadium to trigonal bipyramid.[33] Figure 1b shows the p-brannerite structure of CaV_2O_6 which consists of CaO_6 and VO_5 polyhedra. CuV_2O_6 adopts a t-brannerite structure (Fig. 1c) which is a distorted m-brannerite structure that is stabilized by the Jahn-Teller effect.[33–35] It consists of CuO_6 and VO_6 octahedral layers. At temperatures above 625 °C, CuV_2O_6 transforms from t-brannerite to m-brannerite.[33,35]

The purity and composition of the samples prepared via SCS were evaluated using the ICP-AES method as shown in Table II. The sample compositions matched well with the expected values from the precursor amounts added, including both the end members and the solid solutions, within the limits of experimental uncertainty. The combustion synthesis yields were consistently high, with a range of 95% to 98% for all the samples. These findings suggest that SCS can produce phase-pure products, consistent with our previous findings on the Cu-V-O family.[1,16]

The PXRD patterns for the synthesized compounds are shown in Fig. 2. The X-ray diffractograms of the pristine MgV_2O_6, CaV_2O_6, and CuV_2O_6 were consistent with m-berrenerite, p-berrenerite and t-berrenerite structures, respectively, in line with previous reports.[35–37] Rietveld refinement (Fig. S1) confirmed that MgV_2O_6 and CaV_2O_6 adopted a monoclinic structure with *C*2/*m* space group symmetry while CuV_2O_6 adopted a triclinic (space group, $P\bar{1}$) structure. Table S1 shows a summary of the Rietveld refinements with a goodness of fit, χ^2, between 1.06–1.07. The atomic coordinates for the end members CuV_2O_6, MgV_2O_6, CaV_2O_6, and solid solutions $A_{0.1}Cu_{0.9}V_2O_6$ are shown in Table S2. Furthermore, the effect of alkaline earth metal substitution on the local structure of $A_{0.1}Cu_{0.9}V_2O_6$ (A = Mg, Ca) was investigated by X-ray diffraction (Fig. 2b). A triclinic (space group, $P\bar{1}$) structure was maintained for the $A_{0.1}Cu_{0.9}V_2O_6$ solid solutions.

The shift observed in the main diffraction peak located at 29.38° and for the (201) plane (see the rightmost frame in Fig. 2) with

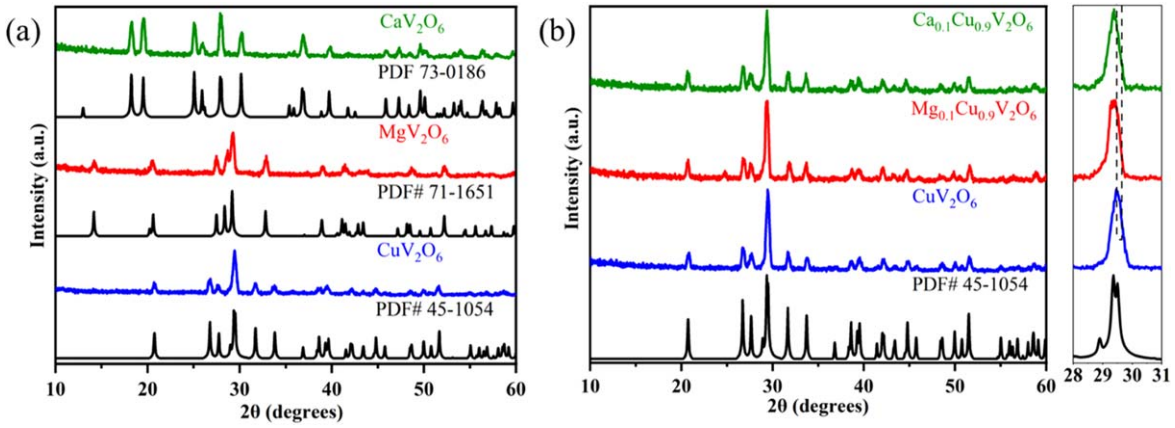

Figure 2. Comparative PXRD patterns for: (a) the end members and their respective reference patterns in black and (b) the solid solutions $A_{0.1}Cu_{0.9}V_2O_6$ and the CuV_2O_6. The panel at extreme right magnifies the peak shift on Mg and Cu alloying.

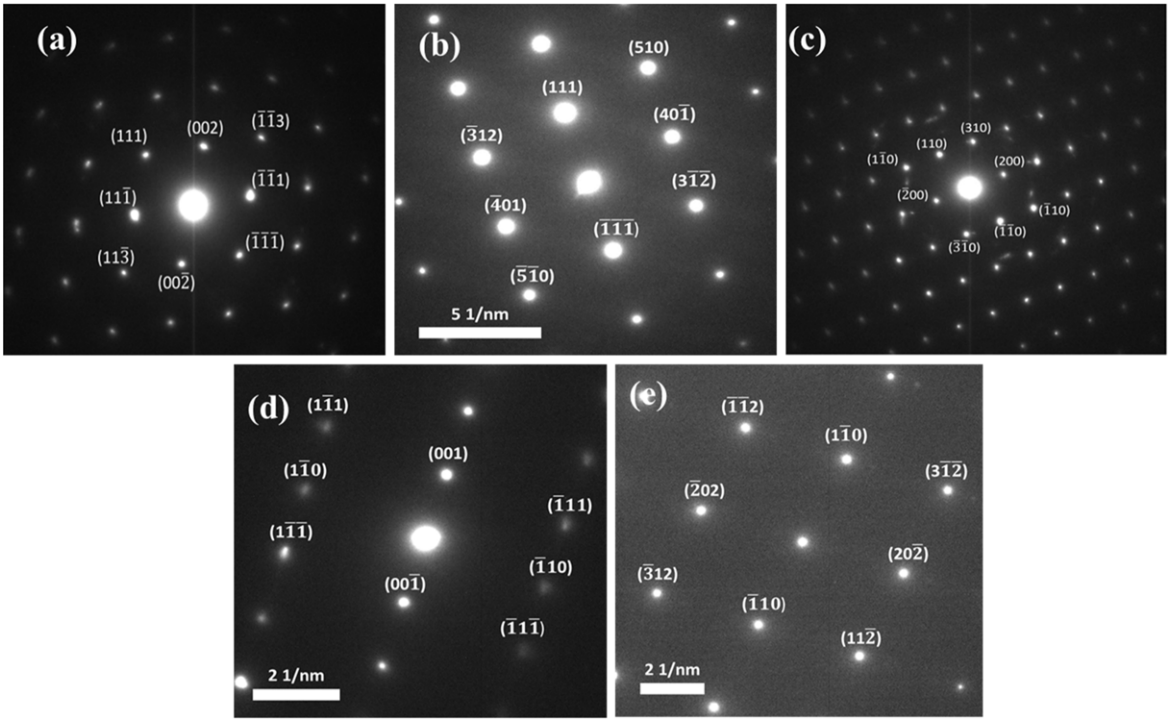

Figure 3. SAED patterns for (a)–(c) the end members MgV_2O_6, CaV_2O_6, CuV_2O_6, and (d), (e) the solid solutions $Mg_{0.1}Cu_{0.9}V_2O_6$ and $Ca_{0.1}Cu_{0.9}V_2O_6$. The SAED spots are indexed to the corresponding unit cells illustrated in Fig. 1.

substitution of copper by the alkaline earth metal, confirms the formation of a solid solution. Specifically, no obvious peaks from either monoclinic MgV_2O_6 or CaV_2O_6 were observed in the PXRD pattern for $A_{0.1}Cu_{0.9}V_2O_6$, also suggesting complete incorporation of Mg or Ca into the CuV_2O_6 lattice. The experimental diffraction patterns for the solid solutions were refined using the Rietveld method (Fig. S1). For the refinement, the occupancy of the mixed A/Cu site (2a) was allowed to "float," and a best fit was observed when 10% of the 2a Wyckoff site was occupied by the alkaline earth metal. The lattice parameters of the solid solution unit cells increased with alkaline earth metal substitution, suggesting the substitution of the small copper atoms by larger alkaline earth metal atoms within the CuV_2O_6 host framework. An attempt to substitute more than 10% of Ca into the CuV_2O_6 lattice yielded a composite mixture (Fig. S2). This is attributed to Ca's large ionic radius compared to Cu's (see Table S3 for the ionic radii). Refinement parameters are listed in Table S1. A small amount (4.4%) of β-$Cu_2V_2O_7$ impurity was detected in the $Mg_{0.1}Cu_{0.9}V_2O_6$ case.

Figure 3 shows selected area electron diffraction (SAED) patterns for the solid solutions and end members. To further confirm alloy formation and phase purity, d-spacing values from SAED patterns of the solid solutions were compared with d-spacings from PXRD data (Table S4). The d-spacing values from the SAED patterns were in good agreement with the corresponding values from Rietveld refinement of the PXRD data. Furthermore, the SAED patterns for the solid solutions showed a regular triclinic symmetric diffraction pattern like for CuV_2O_6.

Figure 4 shows representative SEM images of the solid solutions $A_{0.1}Cu_{0.9}V_2O_6$ in thin film form. A rod-like particle morphology was seen in both Mg and Ca cases. On the other hand, the end members exhibited a variable particle morphology (Fig. S3). The average particle size for the $A_{0.1}Cu_{0.9}V_2O_6$ solid solution samples and for the end members (Fig. S4) were in the range, 2–3 μm but certain particles were larger, around 10 μm. Energy dispersive X-ray (EDX) spectroscopy data are shown in Fig. S5 for the solid solutions. The average Mg/Cu and Ca/Cu ratio was determined to be 0.094 and

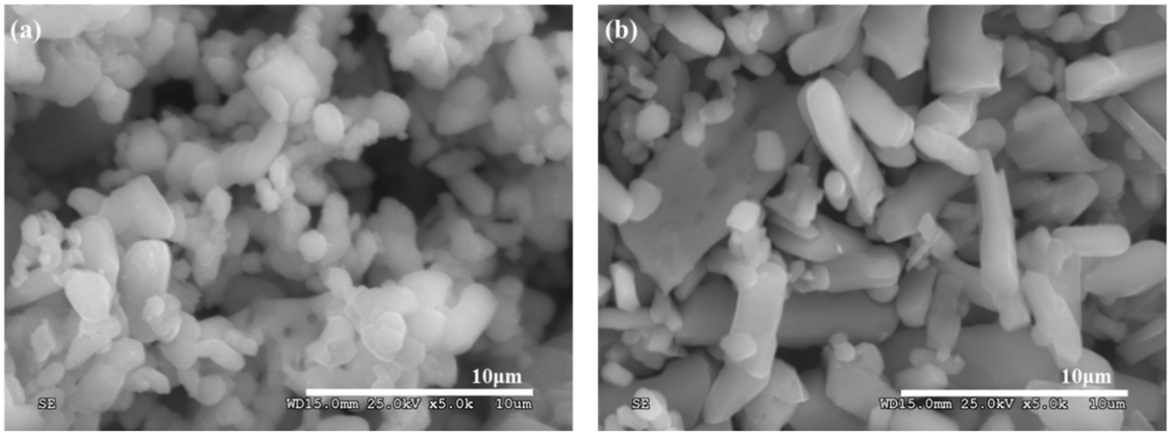

Figure 4. Representative SEM images for (a) $Mg_{0.1}Cu_{0.9}V_2O_6$ and (b) $Ca_{0.1}Cu_{0.9}V_2O_6$.

0.090, respectively, in good agreement with the theoretical stoichiometric value, 0.111 for the chemical formula, $A_{0.1}Cu_{0.9}V_2O_6$. There was uniform distribution of the elements over the various polycrystalline sample grains as shown in the EDX elemental maps in Figs. S6 and S7.

Raman spectra for the end members CuV_2O_6, MgV_2O_6 and CaV_2O_6, and that of the solid solutions $Mg_{0.1}Cu_{0.9}V_2O_6$ and $Ca_{0.1}Cu_{0.9}V_2O_6$ are presented in Fig. 5. The observed Raman bands are in good agreement with previous reports;[16,38] no impurity peaks were observed, again confirming phase purity of these SCS-derived samples. The Raman bands observed in the region 750–950 cm^{-1} were assigned to the stretching vibrations of V–O in the VO_n polyhedra. The bands observed at 400–750 cm^{-1} were assigned to symmetric and asymmetric V–O bending vibrations.[16,38] The Raman bands below 400 cm^{-1} may be assigned to Cu/Mg/Ca–O vibrations and lattice phonon modes.[16,38] While the general shape of the peaks was similar for CuV_2O_6 and $A_{0.1}Cu_{0.9}V_2O_6$ solid solutions, there was noticeable peak shift to the right in the higher wavenumber spectral regime (750–950 cm^{-1}, see rightmost frame, Fig. 5b) upon substitution of Cu by alkaline earth metals, suggesting distortion in VO_6 octahedra due to the axial V−O bond length contraction.

X-ray photoelectron spectra were collected to gain insight into the surface chemical composition and valence states of Mg, Ca, Cu, and V in the end members and the solid solutions. The binding energy range for the core level spectra of Mg 1*s*, Ca 2*p*, and Cu 2*p* appeared in 1300–1308, 340–360, and 925–965 eV, respectively, as seen in Figs. 6a–6c. The divalent oxidation state of Mg was confirmed by the presence of an XPS peak at 1303.8 eV, in good agreement with a previous report on MgO.[39] According to Fig. 6b, the Ca 2*p* core level spectra revealed two peaks at 346.2 and 349.8 eV corresponding to Ca $2p_{3/2}$ and $2p_{1/2}$. A binding energy difference of 3.6 eV, attributable to spin–orbit coupling, confirmed that Ca was in a divalent state.[40] In the XPS spectra for CuV_2O_6, $2p_{3/2}$ and $2p_{1/2}$ peaks with binding energies at 934.4 and 954.3 eV confirm the presence of Cu(II) oxidation state (Fig. 6c). Both the peaks split further into two peaks-931.6/934.4 eV and 951.4/954.3 eV which can be attributed to the presence of Cu^+ ions, and balance the charge associated with oxygen vacancies at the surficial level.[1,41]

The binding energy range for V 2*p* and O 1*s* in MgV_2O_6, CaV_2O_6, and CuV_2O_6, was 510–535 eV as depicted in Figs. 6d–6f. All three end members exhibit spin–orbit splitting for V $2p_{3/2}$ and V $2p_{1/2}$ at 517 and 524.4 eV, respectively, confirming the presence of V^{5+} species.[42] Figures 6d and 6f show the deconvolution of the O 1*s* peaks at three different binding energies i.e., 529.7, 530.4, and 532.5 eV, resulting from the varied bond length with respect to vanadium as the center for MgV_2O_6 and CuV_2O_6.[1,43] Although CaV_2O_6 has three distinct crystallographic sites, only two major peaks were observed for O 1*s* XPS spectra due to the difference in the V-O bond lengths. The lower binding energy peak is due to the occupancy of O2 and O3 having a slight difference in the V-O bond length of 5 pm whereas the higher binding energy peak at 532.5 eV is due to the loosely bonded O1 as compared to the other O atoms.[43] The V-O1, V-O2, and V-O3 bond lengths were 3.67 Å, 1.67 Å, and 1.62 Å respectively, calculated via unit cells produced from the Rietveld refined parameters.

Finally, high-resolution X-ray photoelectron spectra for Mg 1*s*, Ca 2*p*, Cu 2*p*, V 2*p*, and O 1*s* in the $A_{0.1}Cu_{0.9}V_2O_6$ solid solution samples were also collected and deconvoluted, as depicted in Figs. 7a–7f. A good agreement for the oxidation states for metal cations (Ca, Mg, and V) in prepared solid solutions was observed as that of the parent metavanadate composition except for a minor

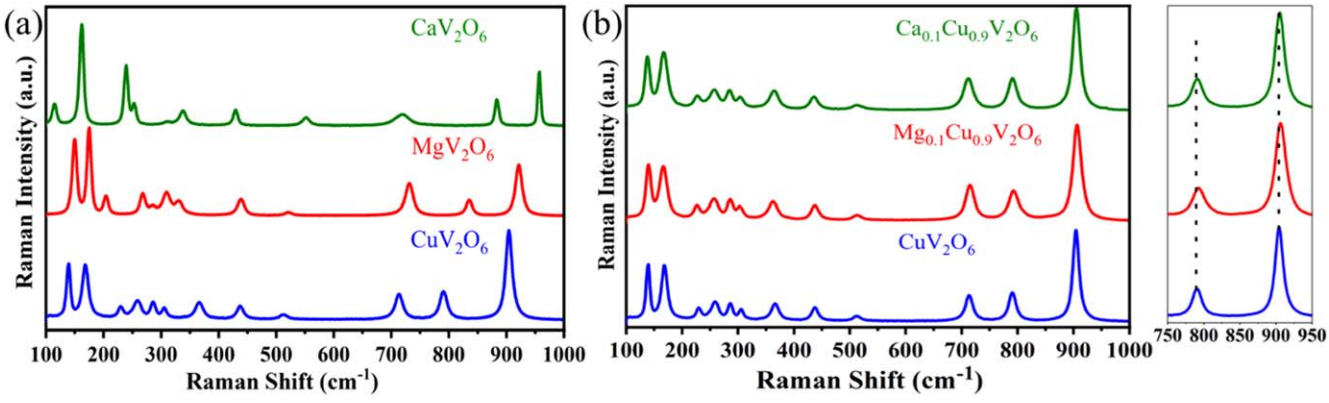

Figure 5. Raman spectra of (a) end members CuV_2O_6, MgV_2O_6, CaV_2O_6 and (b) solid solutions $A_{0.1}Cu_{0.9}V_2O_6$. The panel at extreme right shows an expanded view of the 750–950 spectral region.

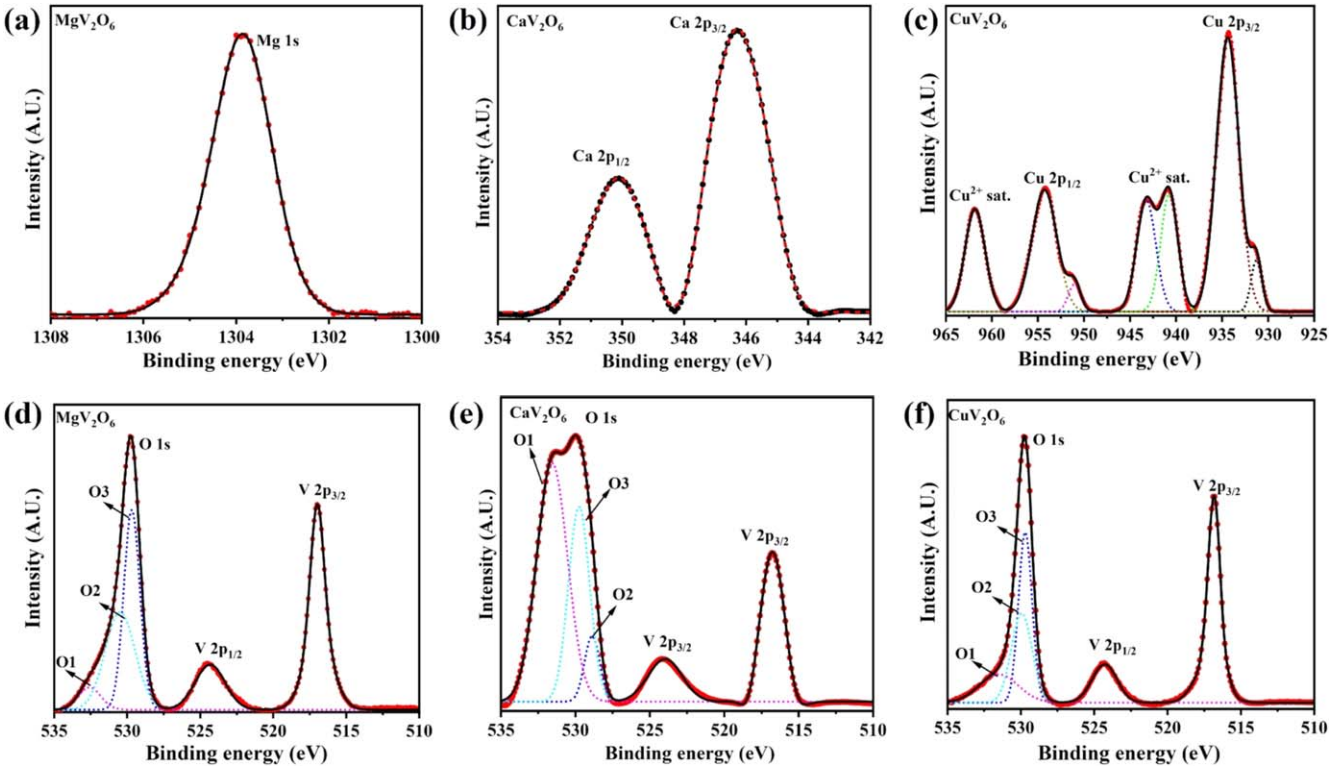

Figure 6. High resolution XPS spectra showing (a) Mg 1*s* in MgV_2O_6, (b) Ca 2*p* in CaV_2O_6, (c) Cu 2*p* in CuV_2O_6 and (d)–(f) O 1*s* and V 2*p* in MgV_2O_6, CaV_2O_6 and CuV_2O_6, respectively. In selected cases, peak deconvolutions are shown.

deviation in the O 1*s* spectra. The change in the hybridization of the Cu-O bond due to the substitution via alkaline earth metal leads to a change in the O atom binding energies. Figure 7c did not show much difference in the O 1*s* spectra from its parent composition except for the O2-O3 binding contribution at the surficial level which is due to the similar size of magnesium as that of copper. On the other hand, calcium owing to its greater ionic radius pulls the intermediate O atom away from vanadium leading to greater binding energy depicted by the emerging peak at 532.5 eV (Fig. 7f). These XPS results explain the distortions in the vanadate polyhedra in the case of $A_{0.1}Cu_{0.9}V_2O_6$ solid solutions. The effect of internal structural distortion is further addressed in the computational data analysis and optical measurement sections respectively.

Electronic band structure calculations.—Geometry optimization was first performed on the unit cells for the end members, CuV_2O_6, MgV_2O_6, and CaV_2O_6 consisting of 18 atoms. Table S5 shows that the DFT-optimized lattice parameters aligned well with the experimentally observed values. However, the optimized lattice parameters for CaV_2O_6 indeed were slightly over-estimated in comparison to the experimental value. This discrepancy may be attributed to utilization of the same Hubbard U value for the 3*d* orbital of V atoms in all three complexes, despite the presence of VO_6 octahedra in CuV_2O_6 and MgV_2O_6 and VO_5 polyhedra in CaV_2O_6. The U value is highly environment-specific inside a crystal and varies with a change in the coordination geometry of an atom; this may have played a role in the slight discrepancy in reproducing the lattice parameters for CaV_2O_6.

Furthermore, to investigate the relative strength of magnetic coupling between the Cu atoms within the unit cell, both ferromagnetic (FM) and antiferromagnetic (AFM) coupling was considered. There existed a discernible disparity in the total energy between the lowest energy AFM and FM structures, amounting to 5.6 meV/Cu atom. This demonstrated a proclivity towards AFM coupling. In any case, the magnetic coupling between the Cu atoms was relatively weak and in good agreement with previous experimental and theoretical observations where the system exhibited paramagnetic behaviour under ambient conditions.[16] Consequently, only the AFM coupling between two neighbouring Cu atoms was considered for all forthcoming DFT computations here.

To investigate the effect of 10% alloying of the host framework, a $1 \times 5 \times 1$ supercell of CuV_2O_6 was considered for the substitution of a Cu atom with either Mg or Ca. Following the atomic substitution, structural optimization was performed, wherein the optimized lattice parameters were determined and tabulated (Table S5). These parameters were in good agreement with the values obtained from experimental measurements. Furthermore, substitution of a Cu atom into $5 \times 1 \times 1$ and $1 \times 1 \times 5$ supercells of CuV_2O_6 also resulted in a doping level of 10%. However, the deviation in total energies assessed through DFT calculations between these two and the $1 \times 5 \times 1$ grid was less than 1 meV/Cu-atom. Therefore, only the $1 \times 5 \times 1$ supercell of CuV_2O_6 was considered for further calculations, which ideally minimized the interaction between two foreign cation sites by maximizing their distances in all the three directions.

Similarly, 12.5% incorporation of the alkaline earth metal was considered to investigate the effects of various types of AFM magnetic couplings between two neighbouring Cu atoms in a $1 \times 2 \times 2$ supercell of $Mg_{0.12}Cu_{0.88}V_2O_6$. From the total energies obtained through DFT calculations, the variation in the formation energy between 10% and 12.5% doping amounted to only 12 meV/Cu site. Consequently, the scenario involving 12.5% alloying was more energetically favorable, though the net magnetic moment as obtained from DFT was 1 μ_B/cell for both 10% and 12.5% alloying. Considering different AFM couplings in 12.5% doping scenario did not significantly affect the formation energy or magnetic moment, hence a 10% alloyed $1 \times 5 \times 1$ supercell of CuV_2O_6 was used for further study.

The electronic band structure in an antiferromagnetically coupled $1 \times 5 \times 1$ supercell of bulk CuV_2O_6 is shown in Fig. 8a while the calculated orbital PDOS of CuV_2O_6 is illustrated in Fig. 8b. As the AFM-coupled Cu atoms led to net zero magnetic moments, a

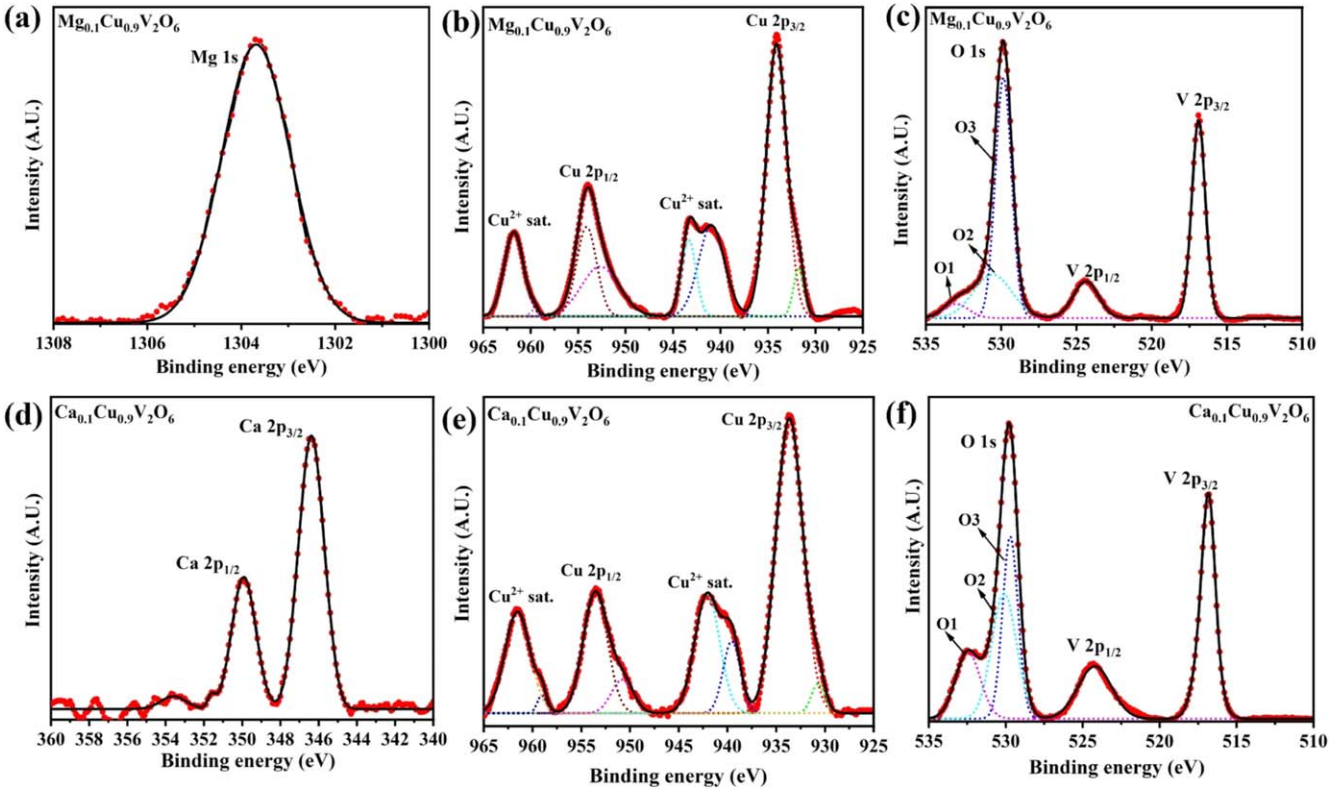

Figure 7. High resolution XPS spectra showing (a)–(c) Mg 1*s*, Cu 2*p,* O 1*s* and V 2*p* in $Mg_{0.1}Cu_{0.9}V_2O_6$, and (d)–(f) Ca 2*p,* Cu 2*p,* O 1*s* and V 2*p* in $Ca_{0.1}Cu_{0.9}V_2O_6$, respectively. In selected cases, peak deconvolutions are also shown.

symmetric band structure was obtained for both spin channels. Thus, in Fig. 8a, only the band structure originating from one spin channel exclusively, is presented. A denser k-point mesh was required to capture the O 2*p* states near the Fermi level. The PDOS plot as displayed in Fig. 8b revealed that hybridized Cu 3*d* and O 2*p* orbitals primarily contributed to the top of the valance band maxima (VBM). The hybridization of Cu *3d* and O *2p* also increased the dispersion at the VBM, thereby presenting an opportunity to reduce the effective mass of the hole/positive charge carriers and hence, improving their mobility. In addition, a mid-gap state was observed in the band structure agreeing with a previous study.[16] These empty mid-gap states are primarily Cu 3*d* e$_{.g.}$ states hybridized with O *2p* orbitals.[31]

In addition, the bottom of the conduction band was mainly occupied by V 3*d* orbitals, which have a minor or negligible contribution from O 2*p* and Cu 3*d* orbitals. From these DFT calculations, CuV_2O_6 was found to be an indirect band gap semiconductor with an energy band gap of 1.84 eV. Comparison with experimental values is deferred to a later section.

Figures 8c and 8e represent the band structure, and Figs. 8d and 8f represent the density of states (DOS) of MgV_2O_6 and CaV_2O_6, respectively. From the PDOS plots of MgV_2O_6 and CaV_2O_6, we note that the *p* and *s* states of the *s*-block alkaline earth metals are not prominent near the Fermi level. Also, these systems do not exhibit mid-gap states in the conduction region. The DFT calculated indirect band gaps were 2.68 eV and 2.85 eV for bulk MgV_2O_6 and CaV_2O_6, respectively.

Figure 9 shows the electronic band structure calculated for both spin-up (red) and spin-down (black) channels in $Mg_{0.1}Cu_{0.9}V_2O_6$ and $Ca_{0.1}Cu_{0.9}V_2O_6$ as well as the calculated orbital PDOS, which were obtained by the substitution of one Cu atom out of ten from an AFM coupled $1 \times 5 \times 1$ supercell of bulk CuV_2O_6. Upon substitution of the Cu atom with elements from the s-block, the system attained a net non-zero magnetic moment because of the presence of an odd number of Cu atoms in a supercell. As expected from the PDOS plots in Figs. 8d and 8f of pristine MgV_2O_6 and CaV_2O_6, we did not observe the contribution of *s* and *p* states of Mg and Ca near the Fermi level in the alloyed systems (see Fig. S8 for the zoomed-in version of Figs. 9b and 9d). In the alloyed systems, we did not observe changes in the mid-gap states as these states were primarily populated by Cu 3*d* states. At the 10% alloying level, the PDOS and the band structure looked like what was observed in Figs. 8a and 8b for unalloyed CuV_2O_6.

The band dispersion of the spin down channel in Figs. 9a and 9c was like the band dispersion observed in Fig. 8a. In contrast, we noticed a slightly modified band dispersion in the spin-up channel near VBM and CBM. The states near VBM were primarily from O 2*p* orbitals; therefore, the modification in band dispersion (near the high symmetry point U) arose from the alloying of Mg and Ca atoms and changes in hybridization of the V-O bonding environment. The absence of Cu at the doping sites, and the introduction of the alkaline earth metal atoms induced a shift in the minimum energy position of neighboring Cu, and V atoms with respect to bulk CuV_2O_6 position, which leads to a change in the vanadium octahedral environment. This change in the vanadium 3*d* octahedral environment due to alloying led to further flattening of the spin-up channel conduction bands (near the high symmetry point R). Moreover, a change in the optical band gap upon Mg alloying was noted for the $Mg_{0.1}Cu_{0.9}V_2O_6$ system; an indirect band gap of 1.85 eV in the spin down channel and 1.90 eV in the spin up channel was noted. Upon Ca alloying in the $Ca_{0.1}Cu_{0.9}V_2O_6$ system, an indirect band gap of 1.87 eV in spin down channel and 1.91 eV in spin up channel, was noted. Experimental measurements of the optical behavior, and photoelectrochemical properties, are discussed next.

Optical and photoelectrochemical behavior.—Diffuse reflectance spectroscopy (DRS) data reveal changes in the optical bandgap of CuV_2O_6 upon substitution of copper by alkaline earth metals. Figure 10a depicts the optical absorption spectra derived from DRS measurements of the end members CuV_2O_6, MgV_2O_6, CaV_2O_6 and solid solutions $A_{0.1}Cu_{0.9}V_2O_6$. The end members CuV_2O_6, MgV_2O_6

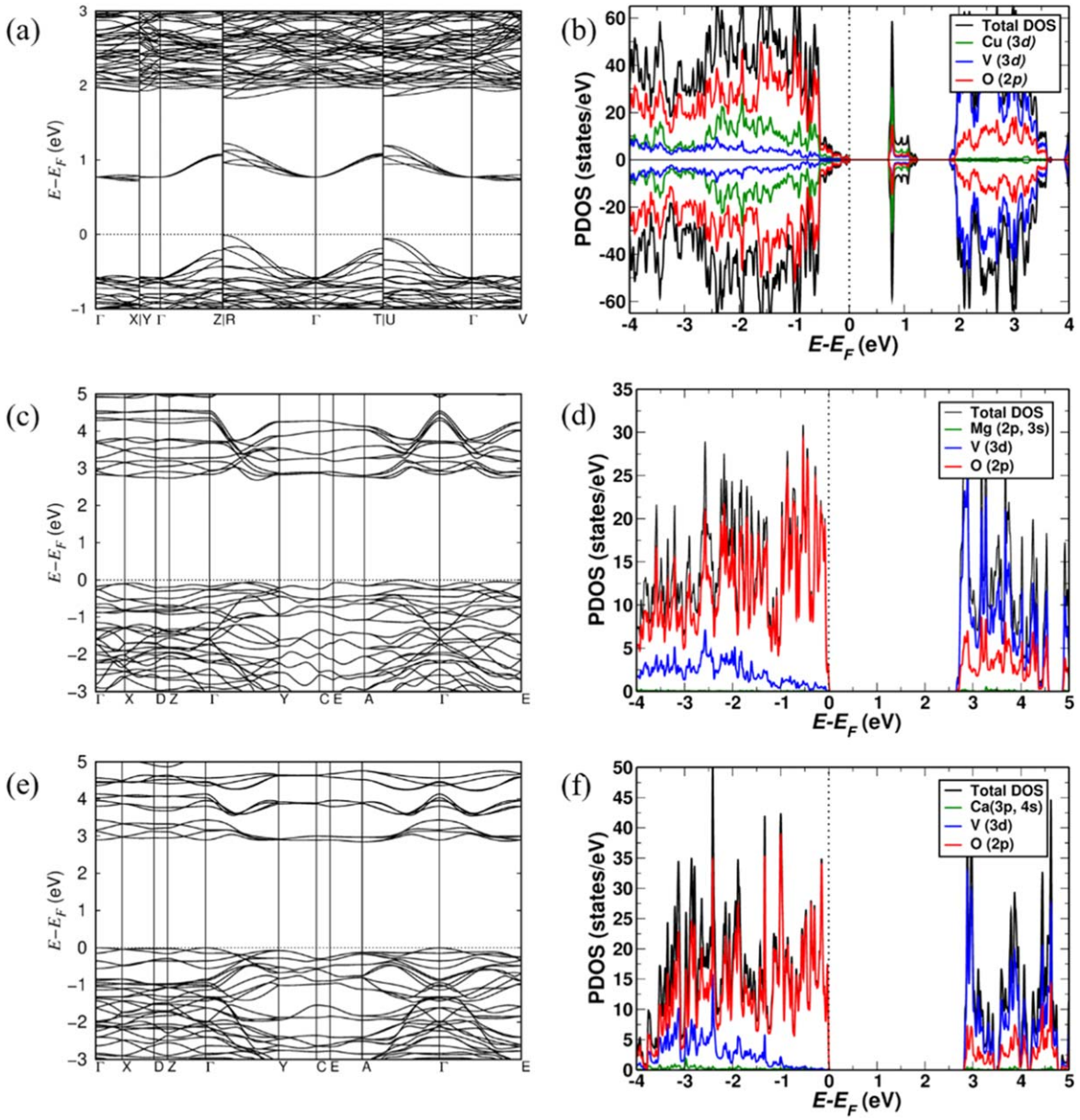

Figure 8. The electronic band structure and projected density of states (PDOS) for the bulk (a), (b) CuV_2O_6, (c), (d) MgV_2O_6 and (e), (f) CaV_2O_6 have been calculated in a $1 \times 5 \times 1$ supercell. The black line represents the total density of states, while the green line displays the projection on Cu 3*d* orbital, Mg 3*s* and 2*p* orbitals, and Ca 4*s* and 3*p* orbitals for the respective compounds. Furthermore, the blue line represents the V 3*d* orbital, and the red line represents the O 2*p* orbital. It is essential to note that the net zero magnetic moment in CuV_2O_6 leads to symmetric band structure with identical band dispersion for both the spin up and spin down channels, hence only one spin channel is shown in the figure.

and CaV_2O_6 exhibited a clear absorption edge at ~700 nm (~1.90 eV), 530 nm (~2.65 eV), and 450 nm (~2.85 eV), respectively. A blue shift in the absorption edge (relative to the unalloyed parent sample) was seen with introduction of alkaline earth metal into the structural framework of CuV_2O_6. Similarly, Tauc plots of the DRS data showed an increase in both direct and indirect bandgaps of CuV_2O_6 upon alloying with 10% alkaline earth metal (Figs. 10b and 10c). This increase in both direct and indirect bandgap can be attributed to changes in the vanadium octahedral environment with introduction of alkaline earth metal.[44]

The PEC activity of CuV_2O_6 and $A_{0.1}Cu_{0.9}V_2O_6$ thin film electrodes were investigated using chopped linear sweep voltammetry (LSV) in 0.1 M borate buffer (pH = 8) under simulated solar light (100 mW cm^{-2}); Fig. 11 shows the results. Both copper vanadate and the solid solutions showed anodic photoactivity under reverse bias potential, diagnostic of *n*-type semiconductor behavior of the photoelectrode films.[45] At the thermodynamic oxidation potential of water (1.23 V vs RHE), the photocurrent density of CuV_2O_6 and $Ca_{0.1}Cu_{0.9}V_2O_6$ was observed at 53 μA cm^{-2} while that of $Mg_{0.1}Cu_{0.9}V_2O_6$ was at 27 μA cm^{-2}. However, the photocurrent density drastically increased beyond 1.23 V vs RHE and achieved a maximum value of 395, 260 and 230 μA cm^{-2} at 1.74 V vs RHE for CuV_2O_6, $Ca_{0.1}Cu_{0.9}V_2O_6$ and $Mg_{0.1}Cu_{0.9}V_2O_6$, respectively (Fig. 11a).

The higher photocurrent density observed in $Ca_{0.1}Cu_{0.9}V_2O_6$ relative to $Mg_{0.1}Cu_{0.9}V_2O_6$ solid solution, can be attributed to a lower bandgap in the former (see above). Consequently, a larger fraction of useful (visible) photons are harnessed in the former. Figure 11b shows an increase in photocurrent density for all samples when the PEC measurements were carried out in borate +4 M formate solution, suggesting faster hole transfer kinetics in the presence of the organic hole scavenger. The photocurrent onset

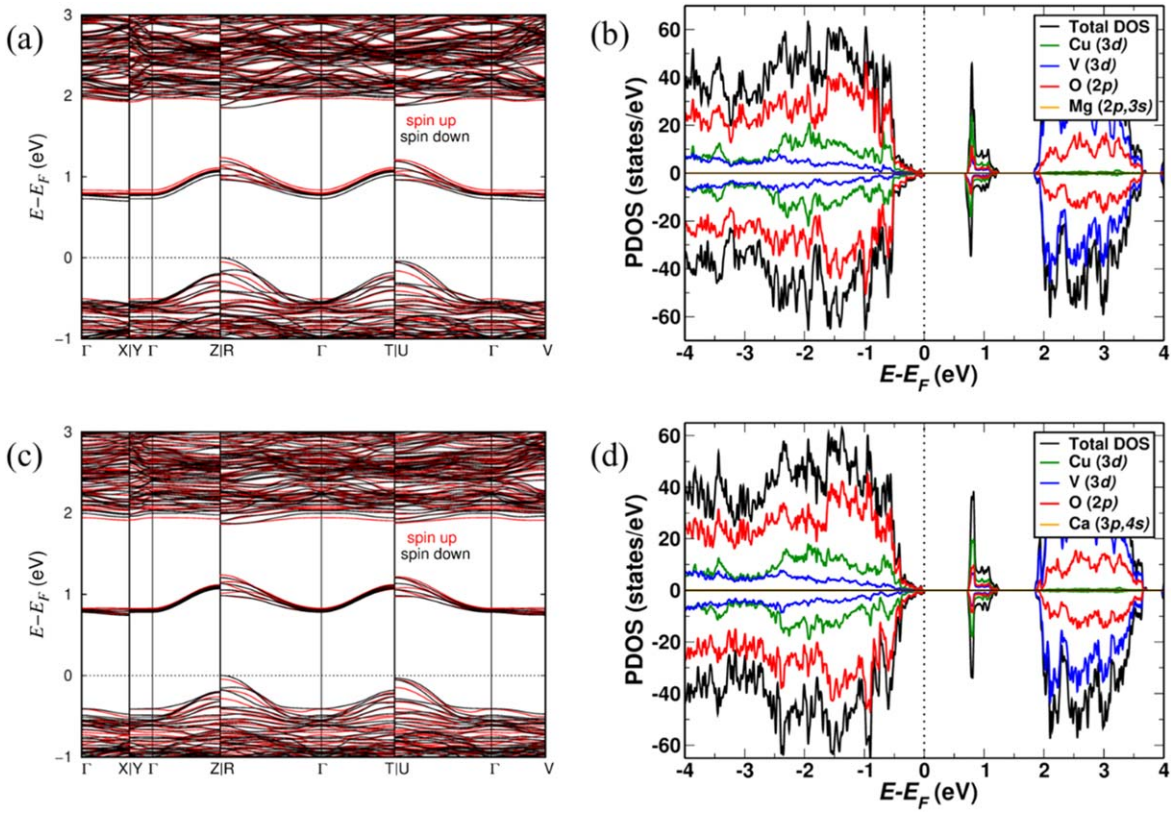

Figure 9. The electronic band structure and projected density of states (PDOS) for (a), (b) $Mg_{0.1}Cu_{0.9}V_2O_6$ and (c), (d) $Ca_{0.1}Cu_{0.9}V_2O_6$ using a $1 \times 5 \times 1$ supercell. The black line represents the total density of states, while the orange line displays the projection on Mg 3*s* and 2*p* orbitals, and Ca 4*s* and 3*p* orbitals for the respective compounds. Furthermore, the green line represents Cu 3*d* orbital, the blue line represents the V 3*d* orbital, and the red line represents the O 2*p* orbital. Note that the system has a net nonzero magnetic moment due to the presence of odd numbers of Cu atoms in the supercell. Both the spin-up (red) and spin-down (black) channels are shown in the band structure plot.

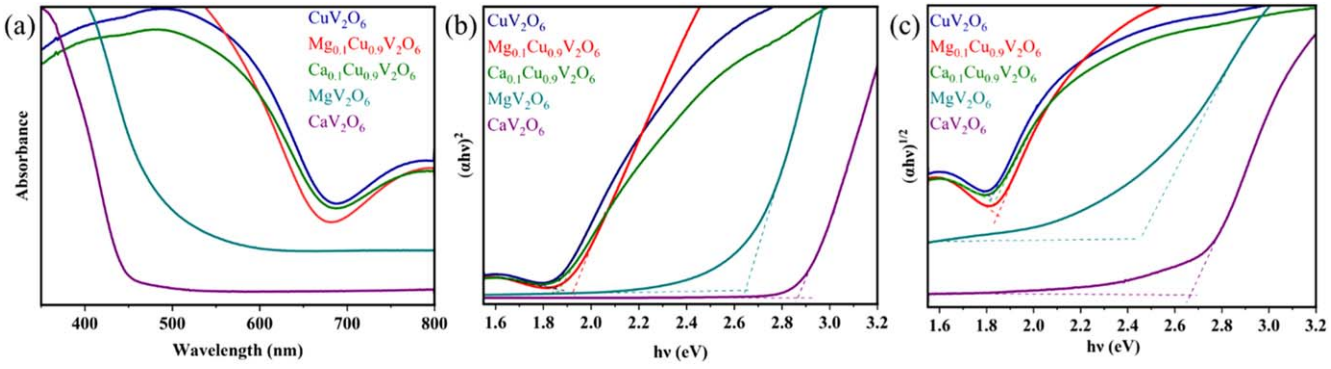

Figure 10. (a) UV-visible optical absorption spectra and Tauc plots corresponding to allowed (b) direct and (c) indirect optical transitions for the end members CuV_2O_6, MgV_2O_6, CaV_2O_6, and for the solid solutions $A_{0.1}Cu_{0.9}V_2O_6$.

potential was also shifted in the negative direction in Fig. 11b relative to Fig. 11a by ~200 mV in line with this notion. The new data on the Ca-alloyed samples reveal the superior PEC behavior relative to the Mg-alloyed samples studied previously.[1]

Conclusions

A combination of theory and experiment involving a diverse range of characterization techniques present a unified and detailed picture of a series of solution combustion derived oxide semiconductors in the A-Cu-V-O (A = Ca, Mg) phase space. Three end members, CaV_2O_6, MgV_2O_6 and CuV_2O_6 and two alloys with the same Cu:A mole ratio were studied. Taken as a whole, the structural, optical, and PEC data are entirely in line with the expectations from the PXRD data, electronic band structure calculations, and the DRS measurements presented in the preceding sections. The values theoretically derived for the optical band gaps were in reasonable agreement with the experimental values in Fig. 10, especially given the well-recognized limitations of the DFT methodology; these comparisons are presented in Table S6. Another trend worth noting is how the disparate ionic radii of Ca vs Mg or Cu (see Table S3), manifest in the corresponding unit cell volumes for the three end members and the two solid solutions (Table S1). Indeed, these trends are broadly in accord; the unit cell volume for CaV_2O_6 is significantly higher than for the other two end members. And the unit cell volume for $Ca_{0.1}Cu_{0.9}V_2O_6$ was higher than that of $Mg_{0.1}Cu_{0.9}V_2O_6$ at a comparable alloying level (Table S1), in line with the larger size of Ca^{2+} vis-à-vis Mg^{2+} (Table S3).

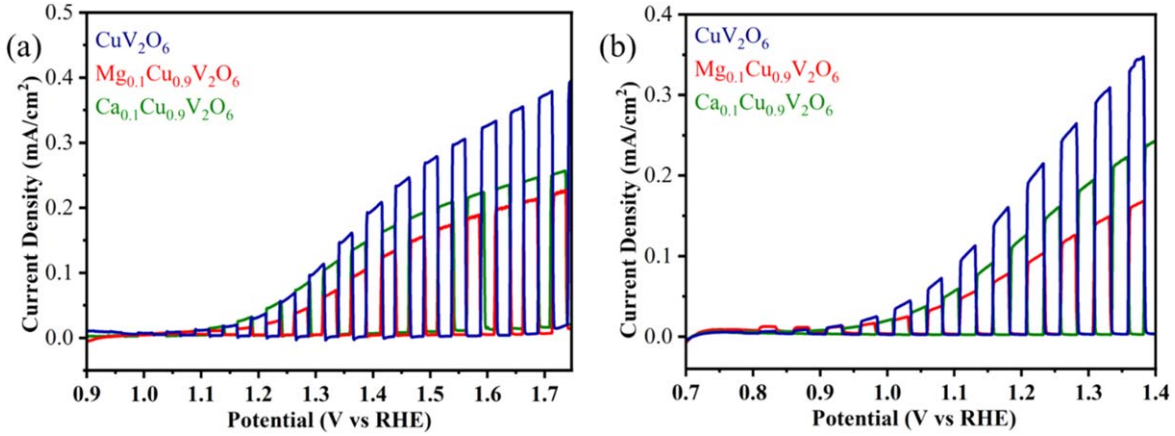

Figure 11. linear sweep photovoltammograms for CuV_2O_6, $Mg_{0.1}Cu_{0.9}V_2O_6$ and $Ca_{0.1}Cu_{0.9}V_2O_6$ in (a) 0.1 M borate buffer solution (pH = 8), (b) 0.1 M borate buffer +4 M formate solution (pH = 8) under front-side illumination. The potential sweep rate was 5 mV s^{-1}.

A major point of this study is that perturbations or distortions in the local structure arising from doping or alloying can have rather profound effects on a macroscopic level in the material's optoelectronic characteristics. Further studies on the solid-state carrier transport and carrier lifetime profiles as a function of the chemical composition, an aspect beyond the scope of this work, would be invaluable to assessment of these new oxide semiconductor alloys for practical technologies.

Acknowledgments

This work was primarily supported by the National Science Foundation UTA/NU Partnership for Research and Education in Materials (DMR-2122128) and the National Science Foundation Materials Research Science and Engineering Center at Northwestern University (NSF DMR-2308691). Elemental analysis was performed at the Northwestern University Quantitative Bio-element Imaging Center. This work made use of the Keck-II facility of Northwestern University's NUANCE Center, which has received support from the SHyNE Resource (NSF ECCS-2025633), the IIN, and Northwestern University's MRSEC program (NSF DMR-2308691). Electronic band structure calculations were performed at the CINECA Supercomputing Center [Convenzione triennale ICTP Anno 2023 (il terzo) Project] under the ISCRA initiative for HPC resources and support.

ORCID

Abhishek Kumar Adak https://orcid.org/0000-0002-6656-5042
Krishnan Rajeshwar https://orcid.org/0000-0003-4917-7790

References

1. A. Rawat et al., "Solution combustion synthesis and characterization of magnesium copper vanadates." *Inorg. Chem.*, **62**, 8903 (2023).
2. S. O'Donnell, C. C. Chung, A. Carbone, R. Broughton, J. L. Jones, and P. A. Maggard, "Pushing the limits of metastability in semiconducting perovskite oxides for visible-light-driven water oxidation." *Chem. Mater.*, **32**, 3054 (2020).
3. S. Ninova, M. Strach, R. Buonsanti, and U. Aschauer, "Suitability of Cu-substituted β-$Mn_2V_2O_7$ and Mn-substituted β-$Cu_2V_2O_7$ for photocatalytic water-splitting." *J. Chem. Phys.*, **153**, 084704 (2020).
4. M. Widenmeyer, T. Kohler, M. Samolis, D. Denko, A. T. Xiao, X. Xie, W. Osterloh, and F. E. Weidenkaff, "Band gap adjustment in perovskite-type $Eu_{1-x}Ca_xTiO_3$ via ammonolysis." *Z. Phys. Chem.*, **234**, 997 (2020).
5. I. Suzuki, Y. Mizuno, and T. Omata, "Tunable direct band gap of β-$CuGaO_2$ and β-$LiGaO_2$ solid solutions in the full visible range." *Inorg. Chem.*, **58**, 4262 (2019).
6. M. Zhang, K. H. Pham, Y. Fang, Y. F. Tay, F. F. Abdi, and L. H. Wong, "The synergistic effect of cation mixing in mesoporous $Bi_xFe_{1-x}VO_4$ heterojunction photoanodes for solar water splitting." *J. Mater. Chem. A*, **7**, 14816 (2019).
7. P. P. Sahoo and P. A. Maggard, "Crystal chemistry, band engineering, and photocatalytic activity of the $LiNb_3O_8$-$CuNb_3O_8$ solid solution." *Inorg. Chem.*, **44**, 4443 (2013).
8. G. F. Samu, Á. Veres, B. Endrődi, E. Varga, K. Rajeshwar, and C. Janáky, "Bandgap-engineered quaternary $M_xBi_{2-x}Ti_2O_7$ (M: Fe, Mn) semiconductor nanoparticles: solution combustion synthesis, characterization, and photocatalysis." *Appl. Catal. B Environ.*, **208**, 148 (2017).
9. S. Eliziario Nunes, C. H. Wang, K. So, J. S.-O. Evans, and I. R. Evans, "Bismuth zinc vanadate, $BiZn_2VO_6$: new crystal structure type and electronic structure." *J. Solid State Chem.*, **222**, 12 (2015).
10. H. Liu, R. Nakamura, and Y. Nakato, "Bismuth copper vanadate $BiCu_2VO_6$ as a novel photocatalyst for efficient visible-light-driven oxygen evolution." *Chem. Phys. Chem*, **6**, 2499 (2005).
11. B. Zoellner, S. O'Donnell, Z. Wu, D. Itanze, A. Carbone, F. E. Osterloh, S. Geyer, and P. A. Maggard, "Impact of Nb(V) substitution on the structure and optical and photoelectrochemical properties of the $Cu_5(Ta_{1-X}Nb_x)_{11}O_{30}$ solid solution." *Inorg. Chem.*, **58**, 6845 (2019).
12. L. Zhou, A. Shinde, P. F. Newhouse, D. Guevarra, Y. Wang, Y. Lai, K. Kan, S. K. Suram, J. A. Haber, and J. M. Gregoire, "Quaternary oxide photosnode discovery improves the spectral response and photovoltage of copper vanadates." *Matter*, **3**, 1 (2020).
13. P. F. Newhouse, D. Guevarra, L. Zhou, Y. Wang, M. Umehara, D. A. Boyd, J. M. Gregoire, and J. A. Haber, "Enhanced bulk transport in copper vanadate photoanodes identified by combinatorial alloying." *Matter*, **3**, 1601 (2020).
14. K. M.-K. Wickramaratne, S. B. Karkai, and F. Ramezanipour, "Electrocatalytic properties of oxygen-deficient perovskites $Ca_3Fe_{3-x}Mn_xO_8$ (x = 1-2) for the hydrogen evolution reaction." *Inorg. Chem.*, **62**, 20961 (2023).
15. M. K. Hossain, P. Sotelo, H. P. Sarker, M. T. Galante, A. Kormányos, C. Longo, R. T. Macaluso, M. N. Huda, C. Janáky, and K. Rajeshwar, "Rapid one-pot synthesis and photoelectrochemical properties of copper vanadates." *ACS Appl. Energy Mater.*, **2**, 2837 (2019).
16. M. K. Hossain et al., "Phase-pure copper vanadate (α-CuV_2O_6): solution combustion synthesis and characterization." *Chem. Mater.*, **32**, 6247 (2020).
17. B. H. Toby, "EXPGUI, a graphical user interface for GSAS." *J. Appl. Crystallogr.*, **34**, 210 (2001).
18. D. Roy, G. F. Samu, M. K. Hossain, C. Janáky, and K. Rajeshwar, "On the measured optical bandgap values of inorganic oxide semiconductors for solar fuels generation." *Catal. Today*, **300**, 136 (2018).
19. J. Tauc, R. Grigorovici, and A. Vancu, "Optical properties and electronic structure of Amorphous Germanium." *Physica Status Solidi (B)*, **15**, 627 (1966).
20. B. D. Viezbicke, S. Patel, B. E. Davis, and D. P. Birnie Iii, "Evaluation of the tauc method for optical absorption edge determination: ZnO thin films as a model system." *Physica Status Solidi. B: Basic Solid-State Physics*, **252**, 1700 (2015).
21. A. B. Murphy, "Band-gap determination from diffuse reflectance measurements of semiconductor films, and application to photoelectrochemical water-splitting." *Sol. Energy Mater. Sol. Cells*, **91**, 1326 (2007).
22. M. K. Hossain, G. F. Samu, K. Gandha, S. Santhanagopalan, J. P. Liu, C. Janáky, and K. Rajeshwar, "Solution combustion synthesis, characterization, and photocatalytic activity of $CuBi_2O_4$ and its nanocomposites with CuO and α-Bi_2O_3." *J. Phys. Chem. C*, **121**, 8252 (2017).
23. P. Giannozzi et al., "Quantum espresso: a modular and open-source software project for quantum simulations of materials." *J. Phys. Condens. Matter*, **21**, 395502 (2009), (19).
24. O. Andreussi et al., "Advanced capabilities for materials modelling with quantum espresso." *Journal of Physics. Condensed Matter*, 465901 (2017).
25. P. E. Blöchl, "Projector augmented-wave method." *Physical Review B*, **50**, 17953 (1994).
26. J. P. Perdew, A. Ruzsinszky, G. I. Csonka, O. A. Vydrov, G. E. Scuseria, L. A. Constantin, X. Zhou, and K. Burke, "Restoring the density-gradient expansion for exchange in solids and surfaces." *Phys. Rev. Lett.*, **100**, 136406 (2008).
27. H. J. Monkhorst and J. D. Pack, "Special points for brillouin-zone integrations." *Physical Review B*, **13**, 5188 (1976).

28. N. Marzari, D. Vanderbilt, A. De Vita, and M. C. Payne, "Thermal contraction and disordering of the Al(110) surface." *Phys. Rev. Lett.*, **82**, 3296 (1999).
29. R. P. Feynman, "Forces in molecules." *Phys. Rev.*, **56**, 340 (1939).
30. A. I. Liechtenstein, V. I. Anisimov, and J. Zaanen, "Density-functional theory and strong interactions: orbital ordering in Mott-Hubbard insulators." *Physical Review B*, **52**, R5467 (1995).
31. J. E. Yourey, K. J. Pyper, J. B. Kurtz, and B. M. Bartlett, "Chemical stability of $CuWO_4$ for photoelectrochemical water oxidation." *The Journal of Physical Chemistry C*, **117**, 8708 (2013).
32. C. M. Tian et al., "Elucidating the electronic structure of $CuWO_4$ thin films for enhanced photoelectrochemical water splitting." *Journal of Materials Chemistry. A, Materials for Energy and Sustainability*, **7**, 11895 (2019).
33. K. Mocała and J. Ziołkowski, "Polymorphism of the bivalent metal vanadates MeV_2O_6 (Me = Mg, Ca, Mn, Co, Ni, Cu, Zn, Cd)." *Journal of Solid-State Chemistry*, **69**, 299 (1987).
34. S. Hong et al., "Local structural disorder in metavanadates MV_2O_6 (M = Zn and Cu) synthesized by the deep eutectic solvent route: photoactive oxides with oxygen vacancies." *Chem. Mater.*, **33**, 1667 (2021).
35. C. Calvo and D. Manolescu, "Refinement of the structure of CuV_2O_6." *Acta Crystallographica Section B*, **29**, 1743 (1973).
36. H. N. Ng and C. Calvo, "Crystal structure of and electron spin resonance of Mn^{2+} in MgV_2O_6." *Can. J. Chem.*, **50**, 3619 (1972).
37. J.-C. Bouloux, G. Perez, and J. Galy, "Structure cristalline des metavanadates CaV_2O_6 et Cd $V_2O_6\alpha$. La lransformation polymorphique $CdV_2O_6\alpha \rightleftarrows CdV_2O_6\beta$." *Bulletin de Minéralogie*, **95**, 130 (1972).
38. X. Jin, X. Ding, Z. Qin, Y. Li, M. Jiao, R. Wang, X. Yang, and X. Lv, "Comprehensive study of electronic, optical, and thermophysical properties of metavanadates CaV_2O_6 and MgV_2O_6." *Inorg. Chem.*, **61**, 17623 (2022).
39. F. Khairallah and A. Glisenti, "XPS study of MgO nanopowders obtained by different preparation procedures." *Surf. Sci. Spectra*, **13**, 58 (2006).
40. G. Manjunath, R. V. Vardhan, A. Salian, R. Jagannatha, M. Kedia, and S. Mandal, "Effect of annealing-temperature-assisted phase evolution on conductivity of solution combustion processed calcium vanadium oxide films." *Bull. Mater. Sci.*, **41**, 1 (2018).
41. Y. Liu, Q. Li, K. Ma, G. Yang, and C. Wang, "Graphene oxide wrapped CuV_2O_6 nanobelts as high-capacity and long-life cathode materials of aqueous zinc-ion batteries." *ACS Nano*, **13**, 12081 (2019).
42. L. Zhou, Q. Yan, A. Shinde, D. Guevarra, P. F. Newhouse, N. Becerra-Stasiewicz, S. M. Chatman, J. A. Haber, J. B. Neaton, and J. M. Gregoire, "High throughput discovery of solar fuels photoanodes in the CuO-V_2O_5 system." *Adv. Energy Mater.*, **5**, 1500968 (2015).
43. R. Yu, N. Xue, S. Huo, J. Li, and J. Wang, "Structure characteristics and photoactivity of simultaneous luminescence and photocatalysis in CaV_2O_6 nanorods synthesized by the Sol-Gel pechini method." *RSC Adv.*, **5**, 6352 (2015).
44. N. Lakshminarasimhan, J. Li, H.-C. Hsu, and M. A. Subramanian, "Optical properties of brannerite-type vanadium oxides, MV_2O_6 (M = Ca, Mg, Mn, Co, Ni, Cu, or Zn)." *Journal of Solid-State Chemistry*, **312**, 123279 (2022).
45. K. Rajeshwar, "Semiconductor electrodes and photoelectrochemistry." *Encyclopedia of Electrochemistry*, ed. S. Licht (Wiley-VCH, Weinheim) 3 (2001), Chap 1 10.1002/9783527610426.bard060001.